Simscape Model - Nano Hexapod

Dehaeze Thomas

February 12, 2025

Contents

Now that the multi-body model of the micro-station has been developed and validated using dynamical measurements, a model of the active vibration platform can be integrated.

First, the mechanical architecture of the active platform needs to be carefully chosen. In Section 1, a quick review of active vibration platforms is performed.

The chosen architecture is the Stewart platform, which is presented in Section 2. It is a parallel manipulator that require the use of specific tools to study its kinematics.

However, to study the dynamics of the Stewart platform, the use of analytical equations is very complex. Instead, a multi-body model of the Stewart platform is developed (Section 3), that can then be easily integrated on top of the micro-station's model.

From a control point of view, the Stewart platform is a MIMO system with complex dynamics. To control such system, it requires several tools to study interaction (Section 4).

1 Active Vibration Platforms

Goals:

- Quick review of active vibration platforms (5 or 6DoF) similar to NASS
- Explain why Stewart platform architecture is chosen
- Wanted controlled DOF: Y, Z, Ry
- But because of continuous rotation (key specificity): X,Y,Z,Rx,Ry in the frame of the active platform
- Literature review? (**maybe more suited for chapter 2**)
  - file:///home/thomas/Cloud/work-projects/ID31-NASS/matlab/stewart-simscape/org/bibliography.org
  - Talk about flexible joint? Maybe not so much as it should be topic of second chapter. Just say that we must of flexible joints that can be defined as 3 to 6DoF joints, and it will be optimize in chapter 2.
- [1]
- For some systems, just XYZ control (stack stages), example: holler
- For other systems, Stewart platform (ID16a), piezo based
- Examples of Stewart platforms for general vibration control, some with Piezo, other with Voice coil. IFF, ... Show different geometry configuration
- DCM: tripod?

1.1 Active vibration control of sample stages

Review of stages with online metrology for Synchrotrons

- ☐ Talk about external metrology? Maybe not the topic here.
- ☐ Talk about control architecture?
- ☐ Comparison with the micro-station / NASS

1.2 Serial and Parallel Manipulators

Goal:

- Explain why a parallel manipulator is here preferred
- Compact, 6DoF, higher control bandwidth, linear, simpler
- Show some example of serial and parallel manipulators
- A review of Stewart platform will be given in Chapter related to the detailed design of the Nano-Hexapod

	Serial Robots	**Parallel Robots**
Advantages	Large Workspace	High Stiffness
Disadvantages	Low Stiffness	Small Workspace
Kinematic Struture	Open	Closed-loop

Table 1.1: Advantages and Disadvantages of both serial and parallel robots

2 The Stewart platform

The Stewart platform, first introduced by Stewart in 1965 [2] for flight simulation applications, represents a significant milestone in parallel manipulator design. This mechanical architecture has evolved far beyond its original purpose, finding applications across diverse fields from precision positioning systems to robotic surgery. The fundamental design consists of two platforms connected by six adjustable struts in parallel, creating a fully parallel manipulator capable of six degrees of freedom motion.

Unlike serial manipulators where errors worsen through the kinematic chain, parallel architectures distribute loads across multiple actuators, leading to enhanced mechanical stiffness and improved positioning accuracy. This parallel configuration also results in superior dynamic performance, as the actuators directly contribute to the platform's motion without intermediate linkages. These characteristics of Stewart platforms have made them particularly valuable in applications requiring high precision and stiffness.

For the NASS application, the Stewart platform architecture presents three key advantages. First, as a fully parallel manipulator, all motion errors of the micro-station can be compensated through the coordinated action of the six actuators. Second, its compact design compared to serial manipulators makes it ideal for integration on top micro-station where only $95\,mm$ of height is available. Third, the good dynamical properties should enable high bandwidth positioning control.

While Stewart platforms excel in precision and stiffness, they typically exhibit a relatively limited workspace compared to serial manipulators. However, this limitation is not significant for the NASS application, as the required motion range corresponds to the positioning errors of the micro-station which are in the order of $10\,\mu m$.

This section provides a comprehensive analysis of the Stewart platform's properties, focusing on aspects crucial for precision positioning applications. The analysis encompasses the platform's kinematic relationships (Section 2.2), the use of the Jacobian matrix (Section 2.3), static behavior (Section 2.4), and dynamic characteristics (Section 2.5). These theoretical foundations form the basis for subsequent design decisions and control strategies, which will be elaborated in later sections.

2.1 Mechanical Architecture

The Stewart platform consists of two rigid platforms connected by six struts arranged in parallel (Figure 2.1). Each strut incorporates an active prismatic joint that enables controlled length variation, with its ends attached to the fixed and mobile platforms through joints. The typical configuration consists of a universal joint at one end and a spherical joint at the other, providing the necessary degrees of freedom[1].

To facilitate rigorous analysis of the Stewart platform, four reference frames are defined:

[1] Different architecture exists, typically referred as "6-SPS" (Spherical, Prismatic, Spherical) or "6-UPS" (Universal, Prismatic, Spherical)

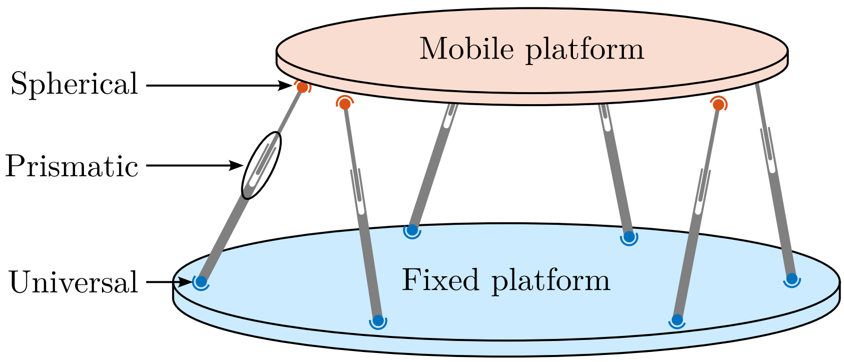

Figure 2.1: Schematical representation of the Stewart platform architecture.

- The fixed base frame $\{F\}$, located at the center of the base platform's bottom surface, serves as the mounting reference for the support structure.
- The mobile frame $\{M\}$, situated at the center of the top platform's upper surface, provides a reference for payload mounting.
- The point-of-interest frame $\{A\}$, fixed to the base but positioned at the workspace center.
- The moving point-of-interest frame $\{B\}$, attached to the mobile platform and coincident with frame $\{A\}$ in the home position.

Frames $\{F\}$ and $\{M\}$ serve primarily to define the joint locations. On the other hand, frames $\{A\}$ and $\{B\}$ are used to describe the relative motion of the two platforms through the position vector ${}^A\boldsymbol{P}_B$ of frame $\{B\}$ expressed in frame $\{A\}$ and the rotation matrix ${}^A\boldsymbol{R}_B$ expressing the orientation of $\{B\}$ with respect to $\{A\}$. For the nano-hexapod, frames $\{A\}$ and $\{B\}$ are chosen to be located at the theoretical focus point of the X-ray light which is $150\,mm$ above the top platform, i.e. above $\{M\}$.

Location of the joints and orientation and length of the struts are crucial for subsequent kinematic, static, and dynamic analyses of the Stewart platform. The center of rotation for the joint fixed to the base is noted $\boldsymbol{a}_i$, while $\boldsymbol{b}_i$ is used for the top platform joints. The struts orientation are represented by the unit vectors $\hat{\boldsymbol{s}}_i$ and their lengths by the scalars l_i. This is summarized in Figure 2.2.

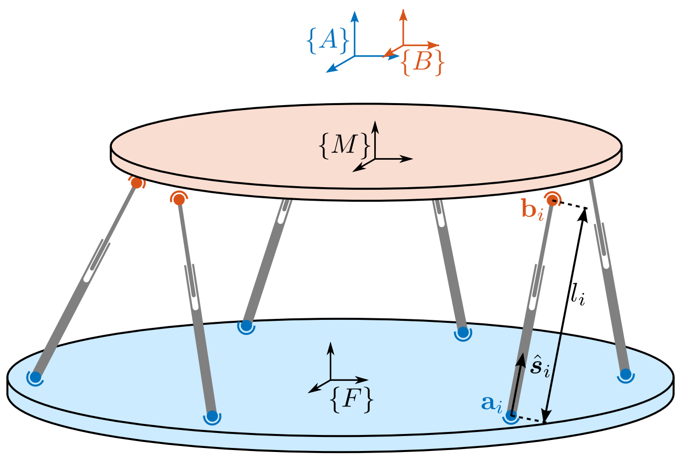

Figure 2.2: Frame and key notations for the Stewart platform

2.2 Kinematic Analysis

The kinematic analysis of the Stewart platform involves understanding the geometric relationships between the platform position/orientation and the actuator lengths, without considering the forces involved.

Loop Closure The foundation of the kinematic analysis lies in the geometric constraints imposed by each strut, which can be expressed through loop closure equations. For each strut i (illustrated in Figure 2.3), the loop closure equation (2.1) can be written.

$$ {}^A\boldsymbol{P}_B = {}^A\boldsymbol{a}_i + l_i {}^A\hat{\boldsymbol{s}}_i - \underbrace{{}^B\boldsymbol{b}_i}_{{}^A\boldsymbol{R}_B {}^B\boldsymbol{b}_i} \quad \text{for } i = 1 \text{ to } 6 \tag{2.1} $$

Such equation links the pose variables ${}^A\boldsymbol{P}$ and ${}^A\boldsymbol{R}_B$, the position vectors describing the known geometry of the base and of the moving platform, $\boldsymbol{a}_i$ and $\boldsymbol{b}_i$, and the strut vector $l_i {}^A\hat{\boldsymbol{s}}_i$:

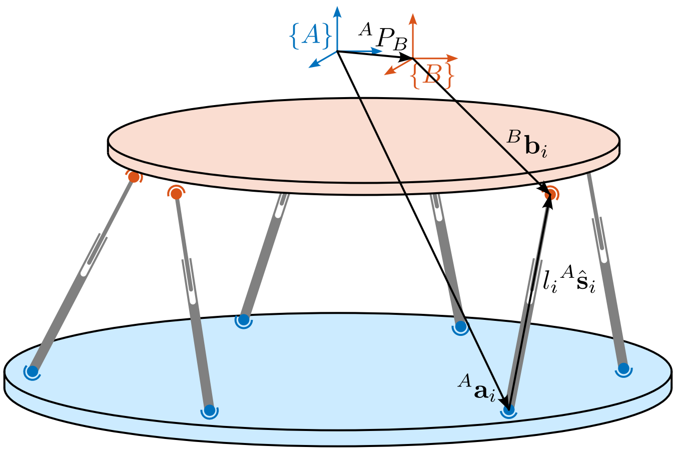

Figure 2.3: Notations to compute the kinematic loop closure

Inverse Kinematics The inverse kinematic problem involves determining the required strut lengths $\boldsymbol{\mathcal{L}} = [l_1, l_2, \dots, l_6]^T$ for a desired platform pose $\boldsymbol{\mathcal{X}}$ (i.e. position ${}^A\boldsymbol{P}$ and orientation ${}^A\boldsymbol{R}_B$). This problem can be solved analytically using the loop closure equations (2.1). The obtain strut lengths are given by (2.2).

$$ l_i = \sqrt{{}^A\boldsymbol{P}^T {}^A\boldsymbol{P} + {}^B\boldsymbol{b}_i^T {}^B\boldsymbol{b}_i + {}^A\boldsymbol{a}_i^T {}^A\boldsymbol{a}_i - 2 {}^A\boldsymbol{P}^T {}^A\boldsymbol{a}_i + 2 {}^A\boldsymbol{P}^T \left[{}^A\boldsymbol{R}_B {}^B\boldsymbol{b}_i \right] - 2 \left[{}^A\boldsymbol{R}_B {}^B\boldsymbol{b}_i \right]^T {}^A\boldsymbol{a}_i} \tag{2.2} $$

If the position and orientation of the platform lie in the feasible workspace, the solution is unique. Otherwise, the solution gives complex numbers.

Forward Kinematics The forward kinematic problem seeks to determine the platform pose $\boldsymbol{\mathcal{X}}$ given a set of strut lengths $\boldsymbol{\mathcal{L}}$. Unlike the inverse kinematics, this presents a significant challenge as it requires solving a system of nonlinear equations. While various numerical methods exist for solving this problem, they can be computationally intensive and may not guarantee convergence to the correct solution.

For the nano-hexapod application, where displacements are typically small, an approximate solution based on linearization around the operating point provides a practical alternative. This approximation, developed in subsequent sections through the Jacobian matrix analysis, proves particularly useful for real-time control applications.

2.3 The Jacobian Matrix

The Jacobian matrix plays a central role in analyzing the Stewart platform's behavior, providing a linear mapping between platform and actuator velocities. While the previously derived kinematic relationships are essential for position analysis, the Jacobian enables velocity analysis and forms the foundation for both static and dynamic studies.

Jacobian Computation - Velocity Loop Closure As was shown in Section 2.2, the strut lengths $\boldsymbol{\mathcal{L}}$ and the platform pose $\boldsymbol{\mathcal{X}}$ are related through a system of nonlinear algebraic equations representing the kinematic constraints imposed by the struts.

By taking the time derivative of the position loop close (2.1), the *velocity loop closure* is obtained (2.3).

$$ {}^A\boldsymbol{v}_p + {}^A\dot{\boldsymbol{R}}_B {}^B\boldsymbol{b}_i + {}^A\boldsymbol{R}_B \underbrace{{}^B\dot{\boldsymbol{b}}_i}_{=0} = \dot{l}_i {}^A\hat{\boldsymbol{s}}_i + l_i {}^A\dot{\hat{\boldsymbol{s}}}_i + \underbrace{{}^A\dot{\boldsymbol{a}}_i}_{=0} \tag{2.3} $$

Moreover, we have:

- ${}^A\dot{\boldsymbol{R}}_B {}^B\boldsymbol{b}_i = {}^A\boldsymbol{\omega} \times {}^A\boldsymbol{R}_B {}^B\boldsymbol{b}_i = {}^A\boldsymbol{\omega} \times {}^A\boldsymbol{b}_i$ in which ${}^A\boldsymbol{\omega}$ denotes the angular velocity of the moving platform expressed in the fixed frame $\{\boldsymbol{A}\}$.
- $l_i {}^A\dot{\hat{\boldsymbol{s}}}_i = l_i \left({}^A\boldsymbol{\omega}_i \times \hat{\boldsymbol{s}}_i\right)$ in which ${}^A\boldsymbol{\omega}_i$ is the angular velocity of strut i express in fixed frame $\{\boldsymbol{A}\}$.

By multiplying both sides by ${}^A\hat{\boldsymbol{s}}_i$, (2.4) is obtained.

$$ {}^A\hat{\boldsymbol{s}}_i {}^A\boldsymbol{v}_p + \underbrace{{}^A\hat{\boldsymbol{s}}_i({}^A\boldsymbol{\omega} \times {}^A\boldsymbol{b}_i)}_{=({}^A\boldsymbol{b}_i \times {}^A\hat{\boldsymbol{s}}_i){}^A\boldsymbol{\omega}} = \dot{l}_i + \underbrace{{}^A\hat{s}_i l_i \left({}^A\boldsymbol{\omega}_i \times {}^A\hat{\boldsymbol{s}}_i\right)}_{=0} \tag{2.4} $$

Equation (2.4) can be rearranged in a matrix form to obtain (2.5), with $\dot{\boldsymbol{\mathcal{L}}} = [\dot{l}_1 \ \dots \ \dot{l}_6]^T$ the vector of strut velocities, and $\dot{\boldsymbol{\mathcal{X}}} = [{}^A\boldsymbol{v}_p, \ {}^A\boldsymbol{\omega}]^T$ the vector of platform velocity and angular velocity.

$$ \boxed{\dot{\boldsymbol{\mathcal{L}}} = \boldsymbol{J}\dot{\boldsymbol{\mathcal{X}}}} \tag{2.5} $$

The matrix $\boldsymbol{J}$ is called the Jacobian matrix, and is defined by (2.6), with:

- ${}^A\hat{\boldsymbol{s}}_i$ the orientation of the struts expressed in $\{A\}$
- ${}^A\boldsymbol{b}_i$ the position of the joints with respect to O_B and express in $\{A\}$

$$\boldsymbol{J} = \begin{bmatrix} {{}^A\hat{\boldsymbol{s}}_1}^T & ({}^A\boldsymbol{b}_1 \times {}^A\hat{\boldsymbol{s}}_1)^T \\ {{}^A\hat{\boldsymbol{s}}_2}^T & ({}^A\boldsymbol{b}_2 \times {}^A\hat{\boldsymbol{s}}_2)^T \\ {{}^A\hat{\boldsymbol{s}}_3}^T & ({}^A\boldsymbol{b}_3 \times {}^A\hat{\boldsymbol{s}}_3)^T \\ {{}^A\hat{\boldsymbol{s}}_4}^T & ({}^A\boldsymbol{b}_4 \times {}^A\hat{\boldsymbol{s}}_4)^T \\ {{}^A\hat{\boldsymbol{s}}_5}^T & ({}^A\boldsymbol{b}_5 \times {}^A\hat{\boldsymbol{s}}_5)^T \\ {{}^A\hat{\boldsymbol{s}}_6}^T & ({}^A\boldsymbol{b}_6 \times {}^A\hat{\boldsymbol{s}}_6)^T \end{bmatrix} \tag{2.6}$$

This Jacobian matrix $\boldsymbol{J}$ therefore links the rate of change of strut length to the velocity and angular velocity of the top platform with respect to the fixed base through a set of linear equations. However, $\boldsymbol{J}$ needs to be recomputed for every Stewart platform pose as it depends on the actual pose of of the manipulator.

Approximate solution of the Forward and Inverse Kinematic problems For small displacements $\delta\boldsymbol{\mathcal{X}} = [\delta x, \delta y, \delta z, \delta\theta_x, \delta\theta_y, \delta\theta_z]^T$ around an operating point $\boldsymbol{\mathcal{X}}_0$ (for which the Jacobian was computed), the associated joint displacement $\delta\boldsymbol{\mathcal{L}} = [\delta l_1, \delta l_2, \delta l_3, \delta l_4, \delta l_5, \delta l_6]^T$ can be computed using the Jacobian (approximate solution of the inverse kinematic problem):

$$\boxed{\delta\boldsymbol{\mathcal{L}} = \boldsymbol{J}\delta\boldsymbol{\mathcal{X}}} \tag{2.7}$$

Similarly, for small joint displacements $\delta\boldsymbol{\mathcal{L}}$, it is possible to find the induced small displacement of the mobile platform (approximate solution of the forward kinematic problem):

$$\boxed{\delta\boldsymbol{\mathcal{X}} = \boldsymbol{J}^{-1}\delta\boldsymbol{\mathcal{L}}} \tag{2.8}$$

These two relations solve the forward and inverse kinematic problems for small displacement in a *approximate* way. As the inverse kinematic can be easily solved exactly this is not much useful, however, as the forward kinematic problem is difficult to solve, this approximation can be very useful for small displacements.

Range validity of the approximate inverse kinematics The accuracy of the Jacobian-based forward kinematics solution was estimated through a systematic error analysis. For a series of platform positions along the x-axis, the exact strut lengths are computed using the analytical inverse kinematics equation (2.2). These strut lengths are then used with the Jacobian to estimate the platform pose, from which the error between the estimated and true poses can be calculated.

The estimation errors in the x, y, and z directions are shown in Figure 2.4. The results demonstrate that for displacements up to approximately $1\,\%$ of the hexapod's size (which corresponds to $100\,\mu m$ as the size of the Stewart platform is here $\approx 100\,mm$), the Jacobian approximation provides excellent accuracy.

This finding has particular significance for the Nano-hexapod application. Since the maximum required stroke ($\approx 100\,\mu m$) is three orders of magnitude smaller than the stewart platform size ($\approx 100\,mm$), the Jacobian matrix can be considered constant throughout the workspace. It can be computed once at the rest position and used for both forward and inverse kinematics with high accuracy.

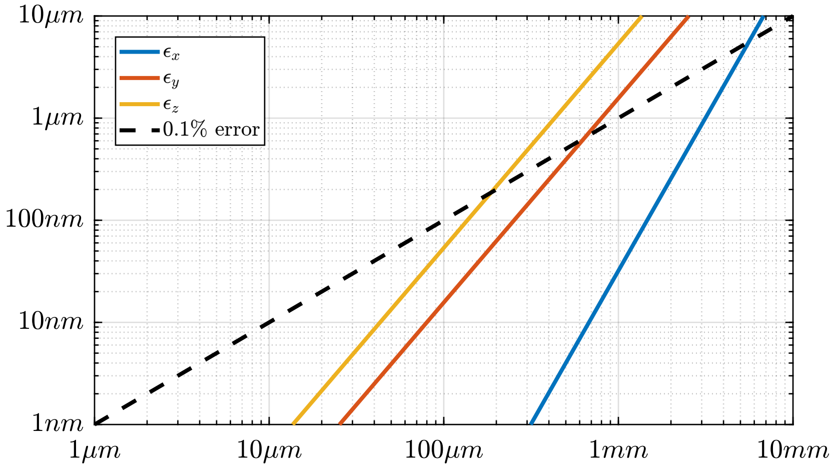

Figure 2.4: Errors associated with the use of the Jacobian matrix to solve the forward kinematic problem. A Stewart platform with an height of 100 mm was used to perform this analysis

Static Forces The static force analysis of the Stewart platform can be elegantly performed using the principle of virtual work. This principle states that, for a system in static equilibrium, the total virtual work of all forces acting on the system must be zero for any virtual displacement compatible with the system's constraints.

Let $\boldsymbol{f} = [f_1, f_2, \cdots, f_6]^T$ represent the vector of actuator forces applied in each strut, and $\boldsymbol{\mathcal{F}} = [\boldsymbol{F}, \boldsymbol{n}]^T$ denote the external wrench (combined force $\boldsymbol{F}$ and torque $\boldsymbol{n}$) acting on the mobile platform at point $\boldsymbol{O}_B$. The virtual work δW consists of two contributions:

- The work performed by the actuator forces through virtual strut displacements $\delta\boldsymbol{\mathcal{L}}$: $\boldsymbol{f}^T\delta\boldsymbol{\mathcal{L}}$
- The work performed by the external wrench through virtual platform displacements $\delta\boldsymbol{\mathcal{X}}$: $-\boldsymbol{\mathcal{F}}^T\delta\boldsymbol{\mathcal{X}}$

The principle of virtual work can thus be expressed as:

$$\delta W = \boldsymbol{f}^T\delta\boldsymbol{\mathcal{L}} - \boldsymbol{\mathcal{F}}^T\delta\boldsymbol{\mathcal{X}} = 0 \tag{2.9}$$

Using the Jacobian relationship that links virtual displacements (2.7), this equation becomes:

$$\left(\boldsymbol{f}^T\boldsymbol{J} - \boldsymbol{\mathcal{F}}^T\right)\delta\boldsymbol{\mathcal{X}} = 0 \tag{2.10}$$

Since this equation must hold for any virtual displacement $\delta\boldsymbol{\mathcal{X}}$, the following force mapping relationships can be derived:

$$\boldsymbol{f}^T\boldsymbol{J} - \boldsymbol{\mathcal{F}}^T = 0 \quad \Rightarrow \quad \boxed{\boldsymbol{\mathcal{F}} = \boldsymbol{J}^T\boldsymbol{f}} \quad \text{and} \quad \boxed{\boldsymbol{f} = \boldsymbol{J}^{-T}\boldsymbol{\mathcal{F}}} \tag{2.11}$$

These equations establish that the transpose of the Jacobian matrix maps actuator forces to platform forces and torques, while its inverse transpose maps platform forces and torques to required actuator forces.

2.4 Static Analysis

The static stiffness characteristics of the Stewart platform play a crucial role in its performance, particularly for precision positioning applications. These characteristics are fundamentally determined by both the actuator properties and the platform geometry.

Starting from the individual actuators, the relationship between applied force f_i and resulting displacement δl_i for each strut i is characterized by its stiffness k_i:

$$f_i = k_i \delta l_i, \quad i = 1, \dots, 6 \tag{2.12}$$

These individual relationships can be combined into a matrix form using the diagonal stiffness matrix $\boldsymbol{\mathcal{K}}$:

$$\boldsymbol{f} = \boldsymbol{\mathcal{K}} \cdot \delta \boldsymbol{\mathcal{L}}, \quad \boldsymbol{\mathcal{K}} = \text{diag}\left[k_1, \dots, k_6\right] \tag{2.13}$$

By applying the force mapping relationships (2.11) derived in the previous section and the Jacobian relationship for small displacements (2.8), the relationship between applied wrench $\boldsymbol{\mathcal{F}}$ and resulting platform displacement $\delta\boldsymbol{\mathcal{X}}$ is obtained (2.14).

$$\boldsymbol{\mathcal{F}} = \underbrace{\boldsymbol{J}^T \boldsymbol{\mathcal{K}} \boldsymbol{J}}_{\boldsymbol{K}} \cdot \delta \boldsymbol{\mathcal{X}} \tag{2.14}$$

where $\boldsymbol{K} = \boldsymbol{J}^T \boldsymbol{\mathcal{K}} \boldsymbol{J}$ is identified as the platform stiffness matrix.

The inverse relationship is given by the compliance matrix $\boldsymbol{C}$:

$$\delta \boldsymbol{\mathcal{X}} = \underbrace{(\boldsymbol{J}^T \boldsymbol{\mathcal{K}} \boldsymbol{J})^{-1}}_{\boldsymbol{C}} \boldsymbol{\mathcal{F}} \tag{2.15}$$

These relationships reveal that the overall platform stiffness and compliance characteristics are determined by two factors:

- The individual actuator stiffnesses represented by $\boldsymbol{\mathcal{K}}$
- The geometric configuration embodied in the Jacobian matrix $\boldsymbol{J}$

This geometric dependency means that the platform's stiffness varies throughout its workspace, as the Jacobian matrix changes with the platform's position and orientation. For the NASS application, where the workspace is relatively small compared to the platform dimensions, these variations can be considered minimal. However, the initial geometric configuration significantly impacts the overall stiffness characteristics. The relationship between maximum stroke and stiffness presents another important design consideration. As both parameters are influenced by the geometric configuration, their optimization involves inherent trade-offs that must be carefully balanced based on application requirements. The optimization of this configuration to achieve desired stiffness properties while having enough stroke will be addressed during the detailed design phase.

2.5 Dynamic Analysis

The dynamic behavior of a Stewart platform can be analyzed through various approaches, depending on the desired level of model fidelity. For initial analysis, we consider a simplified model with the following assumptions:

- Massless struts
- Ideal joints without friction or compliance
- Rigid platform and base

Under these assumptions, the system dynamics can be expressed in the Cartesian space as:

$$\boldsymbol{M} s^2 \boldsymbol{\mathcal{X}} = \Sigma \boldsymbol{\mathcal{F}} \tag{2.16}$$

where $\boldsymbol{M}$ represents the platform mass matrix, $\boldsymbol{\mathcal{X}}$ the platform pose, and $\Sigma\boldsymbol{\mathcal{F}}$ the sum of forces acting on the platform.

The primary forces acting on the system are actuator forces $\boldsymbol{f}$, elastic forces due to strut stiffness $-\boldsymbol{\mathcal{K}}\boldsymbol{\mathcal{L}}$ and damping forces in the struts $\boldsymbol{\mathcal{C}}\dot{\boldsymbol{\mathcal{L}}}$.

$$\Sigma \boldsymbol{\mathcal{F}} = \boldsymbol{J}^T (\boldsymbol{f} - \boldsymbol{\mathcal{K}}\boldsymbol{\mathcal{L}} - s\boldsymbol{\mathcal{C}}\boldsymbol{\mathcal{L}}), \quad \boldsymbol{\mathcal{K}} = \text{diag}(k_1 \ \dots \ k_6), \ \boldsymbol{\mathcal{C}} = \text{diag}(c_1 \ \dots \ c_6) \tag{2.17}$$

Combining these forces and using (2.8) yields the complete dynamic equation (2.18).

$$\boldsymbol{M} s^2 \boldsymbol{\mathcal{X}} = \boldsymbol{\mathcal{F}} - \boldsymbol{J}^T \boldsymbol{\mathcal{K}} \boldsymbol{J} \boldsymbol{\mathcal{X}} - \boldsymbol{J}^T \boldsymbol{\mathcal{C}} \boldsymbol{J} s \boldsymbol{\mathcal{X}} \tag{2.18}$$

The transfer function matrix in the Cartesian frame becomes (2.19).

$$\frac{\mathcal{X}}{\boldsymbol{\mathcal{F}}}(s) = (\boldsymbol{M} s^2 + \boldsymbol{J}^T \boldsymbol{\mathcal{C}} \boldsymbol{J} s + \boldsymbol{J}^T \boldsymbol{\mathcal{K}} \boldsymbol{J})^{-1} \tag{2.19}$$

Through coordinate transformation using the Jacobian matrix, the dynamics in the actuator space is obtained (2.20).

$$\frac{\boldsymbol{\mathcal{L}}}{\boldsymbol{f}}(s) = (\boldsymbol{J}^{-T} \boldsymbol{M} \boldsymbol{J}^{-1} s^2 + \boldsymbol{\mathcal{C}} + \boldsymbol{\mathcal{K}})^{-1} \tag{2.20}$$

While this simplified model provides useful insights, real Stewart platforms exhibit more complex behaviors. Several factors significantly increase model complexity:

- Strut dynamics, including mass distribution and internal resonances
- Joint compliance and friction effects
- Supporting structure dynamics and payload dynamics, which are both very critical for NASS

These additional effects make analytical modeling impractical for complete system analysis.

Conclusion

The fundamental characteristics of the Stewart platform have been analyzed in this chapter. Essential kinematic relationships were developed through loop closure equations, from which both exact and approximate solutions for the inverse and forward kinematic problems were derived. The Jacobian matrix was established as a central mathematical tool, through which crucial insights into velocity relationships, static force transmission, and dynamic behavior of the platform were obtained.

For the NASS application, where displacements are typically limited to the micrometer range, the accuracy of linearized models using a constant Jacobian matrix has been demonstrated, by which both analysis and control can be significantly simplified. However, additional complexities such as strut masses, joint compliance, and supporting structure dynamics must be considered in the full dynamic behavior. This will be performed in the next section using a multi-body model.

All these characteristics (maneuverability, stiffness, dynamics, etc.) are fundamentally determined by the platform's geometry. While a reasonable geometric configuration will be used to validate the NASS during this conceptual phase, the optimization of these geometric parameters will be explored during the detailed design phase.

3 Multi-Body Model

The dynamic modeling of Stewart platforms has traditionally relied on analytical approaches. However, these analytical models become increasingly complex when the full dynamic behavior of struts and joints must be captured. To overcome these limitations, a flexible multi-body approach has been developed that can be readily integrated into the broader NASS system model. Through this multi-body modeling approach, each component model (including joints, actuators, and sensors) can be progressively refined.

The analysis is structured in three parts. First, the multi-body model is developed, wherein detailed geometric parameters, inertial properties, and actuator characteristics are established (Section 3.1). The model is then validated through comparison with analytical equations in a simplified configuration (Section 3.2). Finally, the validated model is employed to analyze the nano-hexapod dynamics, from which insights for the control system design are derived (Section 3.3).

3.1 Model Definition

Geometry The Stewart platform's geometry is defined by two principal coordinate frames (Figure 3.1): a fixed base frame $\{F\}$ and a moving platform frame $\{M\}$. The joints connecting the actuators to these frames are located at positions ${}^F\boldsymbol{a}_i$ and ${}^M\boldsymbol{b}_i$ respectively. The point of interest, denoted by frame $\{A\}$, is situated $150\,mm$ above the moving platform frame $\{M\}$.

The geometric parameters of the nano-hexapod are summarized in Table 3.1. These parameters define the positions of all connection points in their respective coordinate frames. From these parameters, key kinematic properties can be derived: the strut orientations $\hat{\boldsymbol{s}}_i$, strut lengths l_i, and the system's Jacobian matrix $\boldsymbol{J}$.

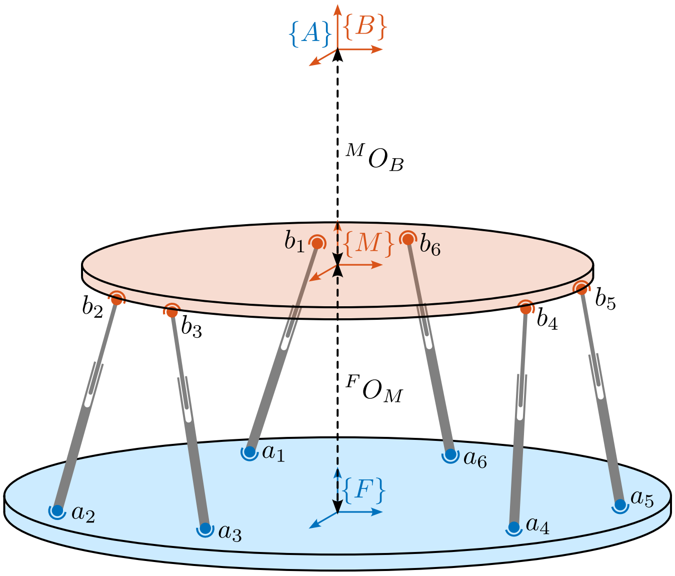

Figure 3.1: Geometry of the stewart platform

	$\boldsymbol{x}$	$\boldsymbol{y}$	$\boldsymbol{z}$
$^M\boldsymbol{O}_B$	0	0	150
$^F\boldsymbol{O}_M$	0	0	95
$^F\boldsymbol{a}_1$	−92	−77	20
$^F\boldsymbol{a}_2$	92	−77	20
$^F\boldsymbol{a}_3$	113	−41	20
$^F\boldsymbol{a}_4$	21	118	20
$^F\boldsymbol{a}_5$	−21	118	20
$^F\boldsymbol{a}_6$	−113	−41	20
$^M\boldsymbol{b}_1$	−28	−106	−20
$^M\boldsymbol{b}_2$	28	−106	−20
$^M\boldsymbol{b}_3$	106	28	−20
$^M\boldsymbol{b}_4$	78	78	−20
$^M\boldsymbol{b}_5$	−78	78	−20
$^M\boldsymbol{b}_6$	−106	28	−20

Table 3.1: Parameter values in [mm]

Inertia of Plates The fixed base and moving platform are modeled as solid cylindrical bodies. The base platform is characterized by a radius of $120\,mm$ and thickness of $15\,mm$, matching the dimensions of the micro-hexapod's top platform. The moving platform is similarly modeled with a radius of $110\,mm$ and thickness of $15\,mm$. Both platforms are assigned a mass of $5\,kg$.

Joints The platform's joints play a crucial role in its dynamic behavior. At both the upper and lower connection points, various degrees of freedom can be modeled, including universal joints, spherical joints, and configurations with additional axial and lateral stiffness components. For each degree of freedom, stiffness characteristics can be incorporated into the model.

In the conceptual design phase, a simplified joint configuration is employed: the bottom joints are modeled as two-degree-of-freedom universal joints, while the top joints are represented as three-degree-of-freedom spherical joints. These joints are considered massless and exhibit no stiffness along their degrees of freedom.

Actuators The actuator model comprises several key elements (Figure 3.2). At its core, each actuator is modeled as a prismatic joint with internal stiffness k_a and damping c_a, driven by a force source f. Similarly to what was found using the rotating 3-DoF model, a parallel stiffness k_p is added in parallel with the force sensor to ensure stability when considering spindle rotation effects.

Each actuator is equipped with two sensors: a force sensor providing measurements f_n and a relative motion sensor measuring strut length l_i. The actuator parameters used in the conceptual phase are presented in Table 3.2.

This modular approach to actuator modeling allows for future refinements as the design evolves, enabling the incorporation of additional dynamic effects or sensor characteristics as needed.

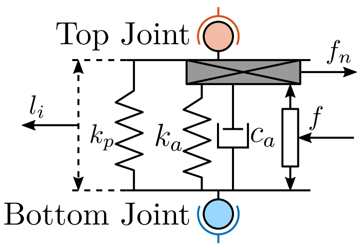

Figure 3.2: Model of the nano-hexapod actuators

	Value
k_a	$1\,N/\mu m$
c_a	$50\,N/(m/s)$
k_p	$0.05\,N/\mu m$

Table 3.2: Actuator parameters

3.2 Validation of the multi-body model

The developed multi-body model of the Stewart platform is represented schematically in Figure 3.3, highlighting the key inputs and outputs: actuator forces $\boldsymbol{f}$, force sensor measurements $\boldsymbol{f}_n$, and relative displacement measurements $\boldsymbol{\mathcal{L}}$. The frames $\{F\}$ and $\{M\}$ serve as interfaces for integration with other elements in the multi-body system. A three-dimensional visualization of the model is presented in Figure 3.4.

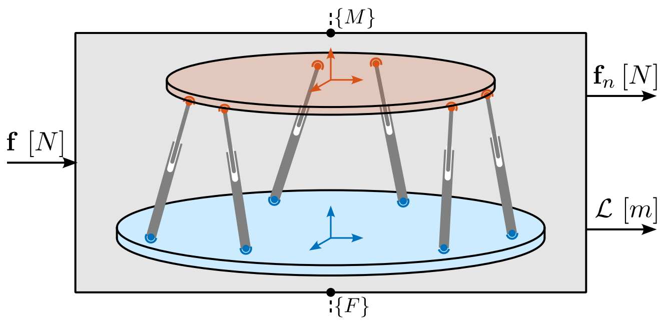

Figure 3.3: Nano-Hexapod plant with inputs and outputs. Frames $\{F\}$ and $\{M\}$ can be connected to other elements in the multi-body models.

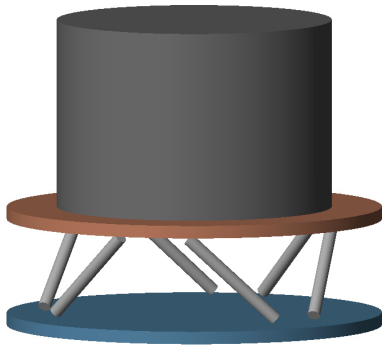

Figure 3.4: 3D representation of the multi-body model

The validation of the multi-body model is performed using the simplest Stewart platform configuration, enabling direct comparison with the analytical transfer functions derived in Section 2.5. This configuration consists of massless universal joints at the base, massless spherical joints at the top platform, and massless struts with stiffness $k_a = 1\,\text{N}/\mu\text{m}$ and damping $c_a = 10\,\text{N}/(\text{m/s})$. The geometric parameters remain as specified in Table 3.2.

While the moving platform itself is considered massless, a 10 kg cylindrical payload is mounted on top with a radius of $r = 110\,mm$ and a height $h = 300\,mm$.

For the analytical model, the stiffness, damping and mass matrices are defined in (3.1).

$$\boldsymbol{\mathcal{K}} = \text{diag}(k_a,\ k_a,\ k_a,\ k_a,\ k_a,\ k_a) \tag{3.1a}$$
$$\boldsymbol{\mathcal{C}} = \text{diag}(c_a,\ c_a,\ c_a,\ c_a,\ c_a,\ c_a) \tag{3.1b}$$
$$\boldsymbol{M} = \text{diag}\left(m,\ m,\ m,\ \frac{1}{12}m(3r^2+h^2),\ \frac{1}{12}m(3r^2+h^2),\ \frac{1}{2}mr^2\right) \tag{3.1c}$$

The transfer functions from actuator forces to strut displacements are computed using these matrices according to equation (2.20). These analytical transfer functions are then compared with those extracted from the multi-body model. The multi-body model yields a state-space representation with 12 states, corresponding to the six degrees of freedom of the moving platform.

Figure 3.5 presents a comparison between the analytical and multi-body transfer functions, specifically showing the response from the first actuator force to all six strut displacements. The close agreement between both approaches across the frequency spectrum validates the multi-body model's accuracy in capturing the system's dynamic behavior.

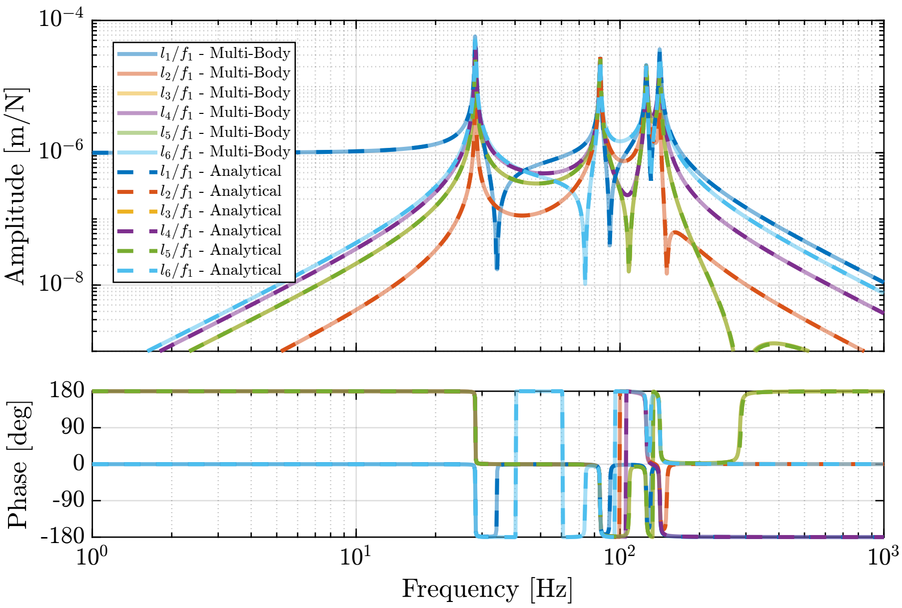

Figure 3.5: Comparison of the analytical transfer functions and the multi-body model

3.3 Nano Hexapod Dynamics

Following the validation of the multi-body model, a detailed analysis of the nano-hexapod dynamics has been performed. The model parameters are set according to the specifications outlined in Section 3.1, with a payload mass of $10\,kg$. Transfer functions from actuator forces $\boldsymbol{f}$ to both strut displacements $\boldsymbol{\mathcal{L}}$ and force measurements $\boldsymbol{f}_n$ are derived from the multi-body model.

The transfer functions relating actuator forces to strut displacements are presented in Figure 3.6a. Due to the system's symmetrical design and identical strut configurations, all diagonal terms (transfer functions from force f_i to displacement l_i of the same strut) exhibit identical behavior. While the system possesses six degrees of freedom, only four distinct resonance frequencies are observed in the frequency response. This reduction from six to four observable modes is attributed to the system's symmetry, where two pairs of resonances occur at identical frequencies.

The system's behavior can be characterized in three frequency regions. At low frequencies, well below the first resonance, the plant demonstrates good decoupling between actuators, with the response dominated by the strut stiffness: $G(j\omega) \xrightarrow[\omega\to 0]{} \mathcal{K}^{-1}$. In the mid-frequency range, the system exhibits coupled dynamics through its resonant modes, reflecting the complex interactions between the platform's degrees of freedom. At high frequencies, above the highest resonance, the response is governed by the payload's inertia mapped to the strut coordinates: $G(j\omega) \xrightarrow[\omega\to\infty]{} J M^{-T} J^T \frac{-1}{\omega^2}$

The force sensor transfer functions, shown in Figure 3.6b, display characteristics typical of collocated actuator-sensor pairs. Each actuator's transfer function to its associated force sensor exhibits alternating complex conjugate poles and zeros. The inclusion of parallel stiffness introduces an additional complex conjugate zero at low frequency, a feature previously observed in the three-degree-of-freedom rotating model.

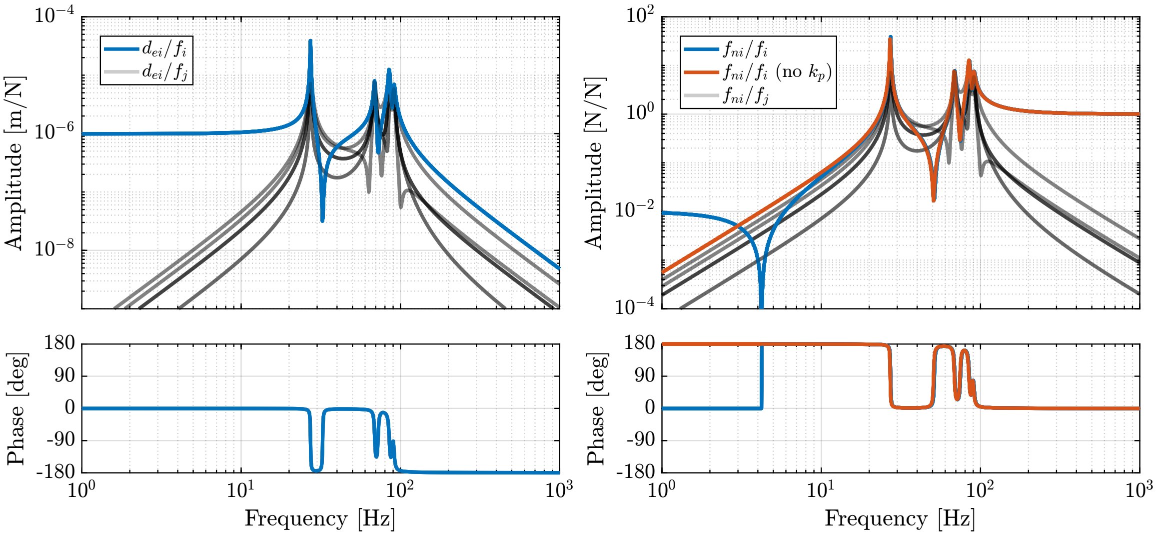

(a) $\boldsymbol{f}$ to $\boldsymbol{d}_L$

(b) $\boldsymbol{f}$ to $\boldsymbol{f}_m$

Figure 3.6: Bode plot of the transfer functions computed from the nano-hexapod multi-body model

Conclusion

The multi-body modeling approach presented in this section provides a comprehensive framework for analyzing the dynamics of the nano-hexapod system. Through comparison with analytical solutions in a simplified configuration, the model's accuracy has been validated, demonstrating its ability to capture the essential dynamic behavior of the Stewart platform.

A key advantage of this modeling approach lies in its flexibility for future refinements. While the current implementation employs idealized joints for the conceptual design phase, the framework readily accommodates the incorporation of joint stiffness and other non-ideal effects. The joint stiffness, known to impact the performance of decentralized IFF control strategy [3], can be studied as the design evolved and will be optimized during the detail design phase. The validated multi-body model will serve as a valuable tool for predicting system behavior and evaluating control performance throughout the design process.

4 Control of Stewart Platforms

The control of Stewart platforms presents distinct challenges compared to the uniaxial model due to their multi-input multi-output nature. While the uniaxial model demonstrated the effectiveness of the HAC-LAC strategy, its extension to Stewart platforms requires careful consideration discussed in this section.

First, the distinction between centralized and decentralized control approaches is discussed in Section 4.1. The impact of the control space selection - either Cartesian or strut space - is then analyzed in Section 4.2, highlighting the trade-offs between direction-specific tuning and implementation simplicity.

Building upon these analyses, a decentralized active damping strategy using Integral Force Feedback is developed in Section 4.3, followed by the implementation of a centralized High Authority Control for positioning in Section 4.4. This architecture, while simple, will be used to demonstrate the feasibility of the NASS concept and will provide a foundation for more sophisticated control strategies to be developed during the detailed design phase.

4.1 Centralized and Decentralized Control

In the control of MIMO systems and more specifically of Stewart platforms, a fundamental architectural decision lies in the choice between centralized and decentralized control strategies.

In decentralized control, each actuator operates based on feedback from its associated sensor only, creating independent control loops as illustrated in Figure 4.1. While mechanical coupling between the struts exists, the control decisions are made locally, with each controller processing information from a single sensor-actuator pair. This approach offers simplicity in implementation and reduced computational requirements.

Conversely, centralized control utilizes information from all sensors to determine the control action for each actuator. This strategy potentially enables better performance by explicitly accounting for the mechanical coupling between the struts, though at the cost of increased complexity in both design and implementation.

The choice between these approaches depends significantly on the degree of interaction between the different control channels, but also on the available sensors and actuators. For instance, when using external metrology systems that measure the platform's global position, centralized control becomes necessary as each sensor measurement depends on all actuator inputs.

In the context of the nano-hexapod, two distinct control strategies will be examined during the conceptual phase:

- Decentralized Integral Force Feedback (IFF), which utilizes collocated force sensors to implement independent control loops for each strut (Section 4.3)

- High-Authority Control (HAC), which employs a centralized approach to achieve precise positioning based on external metrology measurements (Section 4.4)

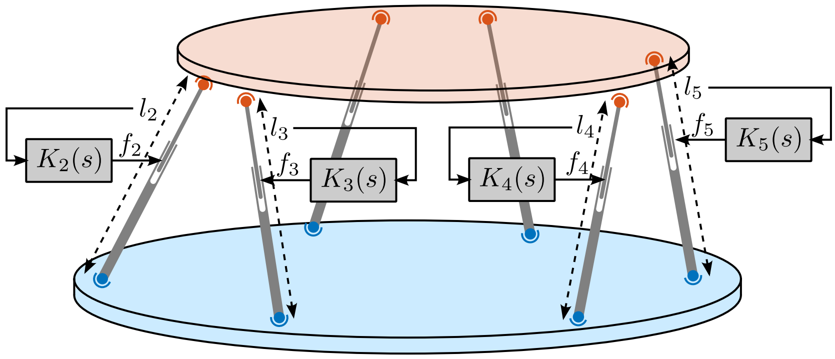

Figure 4.1: Decentralized control strategy using the encoders. The two controllers for the struts on the back are not shown for simplicity.

4.2 Choice of the Control Space

When controlling a Stewart platform using external metrology that measures the pose of frame $\{B\}$ with respect to $\{A\}$, denoted as $\boldsymbol{\mathcal{X}}$, the control architecture can be implemented in either Cartesian space or strut space. This choice impacts both the control design and the obtained performance.

Control in the Strut space In this approach, illustrated in Figure 4.2a, the control is performed in the space of the struts. The Jacobian matrix is used to solve the inverse kinematics in real-time, mapping position errors from Cartesian space $\boldsymbol{\epsilon}_{\mathcal{X}}$ to strut space $\boldsymbol{\epsilon}_{\mathcal{L}}$. A diagonal controller then processes these strut-space errors to generate force commands for each actuator.

The main advantage of this approach emerges from the plant characteristics in strut space, as shown in Figure 4.3a. The diagonal terms of the plant (transfer functions from force to displacement of the same strut, as measured by the external metrology) are identical due to the system's symmetry. This simplifies the control design as only one controller needs to be tuned. Furthermore, at low frequencies, the plant exhibits good decoupling between struts, allowing for effective independent control of each axis.

Control in Cartesian Space Alternatively, control can be implemented directly in Cartesian space, as shown in Figure 4.2b. Here, the controller processes Cartesian errors $\boldsymbol{\epsilon}_{\mathcal{X}}$ to generate forces and torques $\boldsymbol{\mathcal{F}}$, which are then mapped to actuator forces through the transpose of the inverse Jacobian matrix.

The plant behavior in Cartesian space, illustrated in Figure 4.3b, reveals interesting characteristics. Some degrees of freedom, particularly the vertical translation and rotation about the vertical axis, exhibit simpler second-order dynamics. A key advantage of this approach is that control performance can be individually tuned for each direction. This is particularly valuable when performance requirements differ between degrees of freedom - for instance, when higher positioning accuracy is required vertically than horizontally, or when certain rotational degrees of freedom can tolerate larger errors than others.

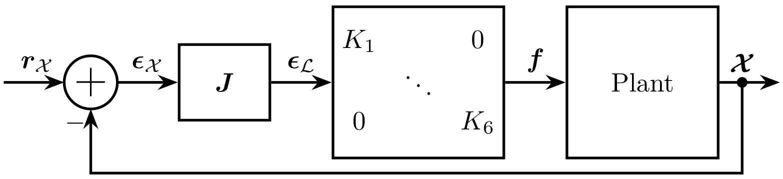

(a) Control in the frame of the struts. $\boldsymbol{J}$ is used to project errors in the frame of the struts

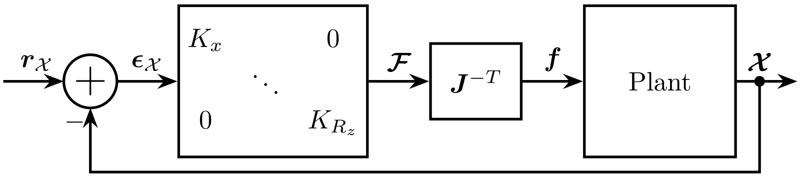

(b) Control in the Cartesian frame. $\boldsymbol{J}^{-T}$ is used to project force and torques on each strut

Figure 4.2: Two control strategies

However, significant coupling exists between certain degrees of freedom, particularly between rotations and translations (e.g., $\epsilon_{R_x}/\mathcal{F}_y$ or ϵ_{D_y}/M_x).

For the conceptual validation of the nano-hexapod, control in the strut space has been selected due to its simpler implementation and the beneficial decoupling properties observed at low frequencies. More sophisticated control strategies will be explored during the detailed design phase.

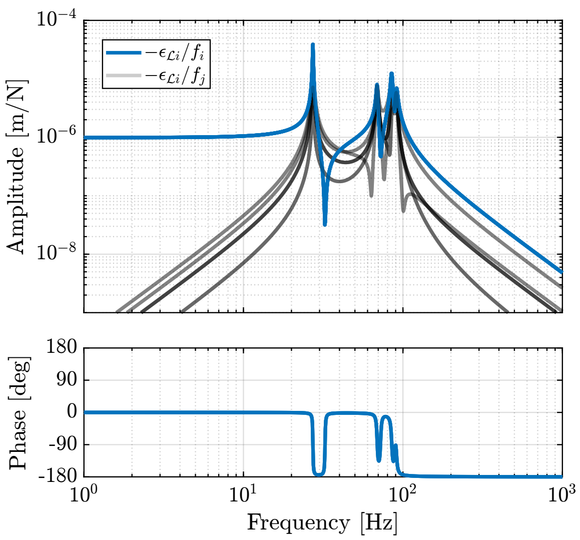

(a) Plant in the frame of the struts

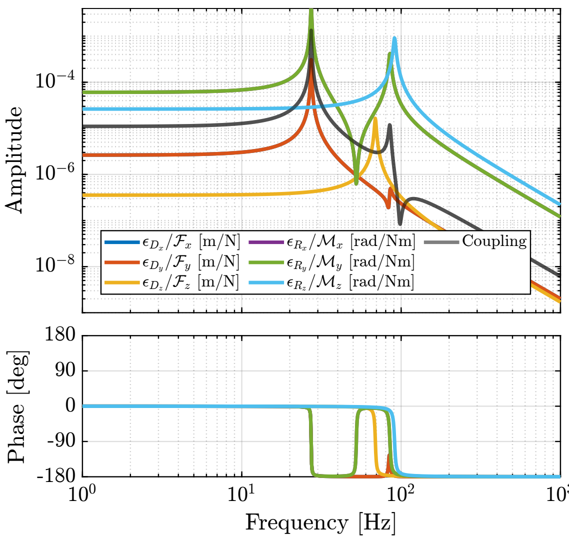

(b) Plant in the Cartesian Frame

Figure 4.3: Bode plot of the transfer functions computed from the nano-hexapod multi-body model

4.3 Active Damping with Decentralized IFF

The decentralized Integral Force Feedback (IFF) control strategy is implemented using independent control loops for each strut, similarly to what is shown in Figure 4.1, but using force sensors instead of relative motion sensors.

The corresponding block diagram of the control loop is shown in Figure 4.4, in which the controller $\boldsymbol{K}_{\text{IFF}}(s)$ is a diagonal matrix where each diagonal element is a pure integrator (4.1).

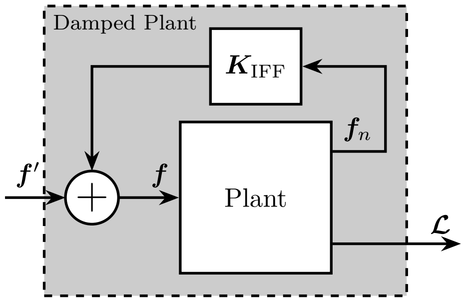

Figure 4.4: Schematic of the implemented decentralized IFF controller. The damped plant has a new inputs $\boldsymbol{f}'$

$$\boldsymbol{K}_{\text{IFF}}(s) = g \cdot \begin{bmatrix} K_{\text{IFF}}(s) & & 0 \\ & \ddots & \\ 0 & & K_{\text{IFF}}(s) \end{bmatrix}, \quad K_{\text{IFF}}(s) = \frac{1}{s} \tag{4.1}$$

In this section, the stiffness in parallel with the force sensor has been omitted since the Stewart platform is not subjected to rotation. The effect of this parallel stiffness will be examined in the next section when the platform is integrated into the complete NASS system.

The Root Locus analysis, shown in Figure 4.5b, reveals the evolution of the closed-loop poles as the controller gain g varies from 0 to ∞. A key characteristic of force feedback control with collocated sensor-actuator pairs is observed: all closed-loop poles are bounded to the left-half plane, indicating guaranteed stability [5]. This property is particularly valuable as the coupling is very large around resonance frequencies, enabling control of modes that would be difficult to include within the bandwidth using position feedback alone.

The bode plot of an individual loop gain (i.e. the loop gain of $K_{\text{IFF}}(s) \cdot \frac{f_{ni}}{f_i}(s)$), presented in Figure 4.5a, exhibits the typical characteristics of integral force feedback of having a phase bounded between -90^o and $+90^o$. The loop-gain is high around the resonance frequencies, indicating that the decentralized IFF provides significant control authority over these modes. This high gain, combined with the bounded phase, enables effective damping of the resonant modes while maintaining stability.

4.4 MIMO High-Authority Control - Low-Authority Control

The design of the High Authority Control positioning loop is now examined. The complete HAC-IFF control architecture is illustrated in Figure 4.6, where the reference signal $\boldsymbol{r}_{\mathcal{X}}$ represents the desired pose, and $\boldsymbol{\mathcal{X}}$ is the measured pose by the external metrology system.

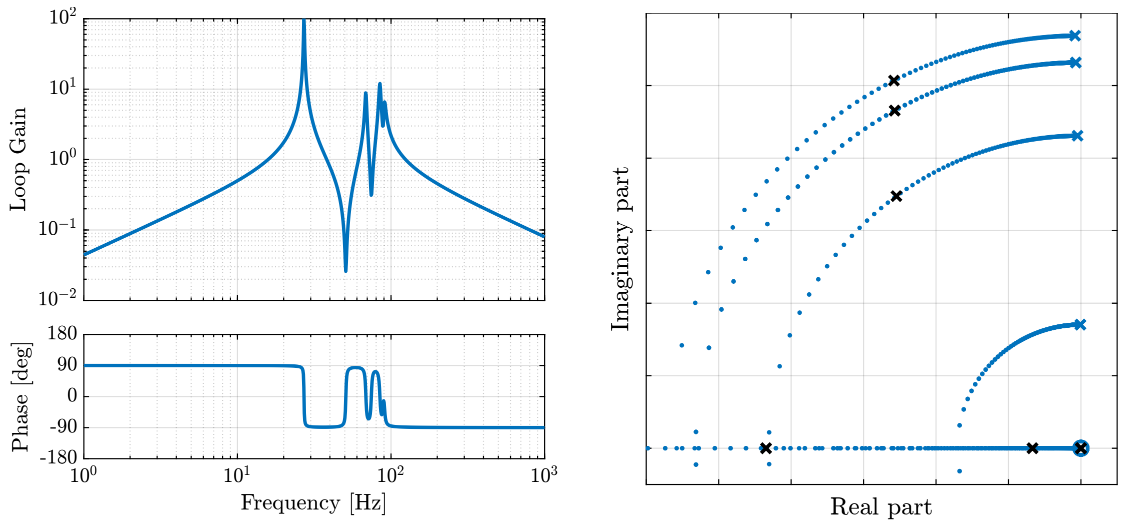

(a) Loop Gain: bode plot of $K_{\text{IFF}}(s)\frac{f_{n1}}{f_1}(s)$

(b) Root Locus

Figure 4.5: Decentralized IFF

Following the analysis from Section 4.2, the control is implemented in the strut space. The Jacobian matrix $\boldsymbol{J}^{-1}$ performs real-time approximate inverse kinematics to map position errors from Cartesian space $\boldsymbol{\epsilon}_{\mathcal{X}}$ to strut space $\boldsymbol{\epsilon}_{\mathcal{L}}$. A diagonal High Authority Controller $\boldsymbol{K}_{\text{HAC}}$ then processes these errors in the frame of the struts.

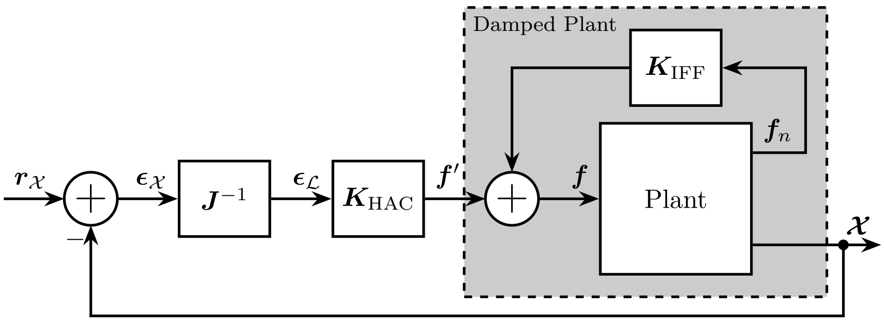

Figure 4.6: HAC-IFF control architecture with the High Authority Controller being implemented in the frame of the struts

The effect of decentralized IFF on the plant dynamics can be observed by comparing two sets of transfer functions. Figure 4.7a shows the original transfer functions from actuator forces $\boldsymbol{f}$ to strut errors $\boldsymbol{\epsilon}_{\mathcal{L}}$, characterized by pronounced resonant peaks. When decentralized IFF is implemented, the transfer functions from modified inputs $\boldsymbol{f}'$ to strut errors $\boldsymbol{\epsilon}_{\mathcal{L}}$, shown in Figure 4.7b, exhibit significantly attenuated resonances. This damping of structural resonances serves two purposes: it reduces vibrations in the vicinity of resonances and simplifies the design of the high authority controller by providing a simpler plant dynamics.

Building upon the damped plant dynamics shown in Figure 4.7b, a high authority controller is designed with the structure given in (4.2). The controller combines three elements: an integrator providing high gain at low frequencies, a lead compensator improving stability margins, and a low-pass filter for robustness to unmodeled high-frequency dynamics. The loop gain of an individual control channel is

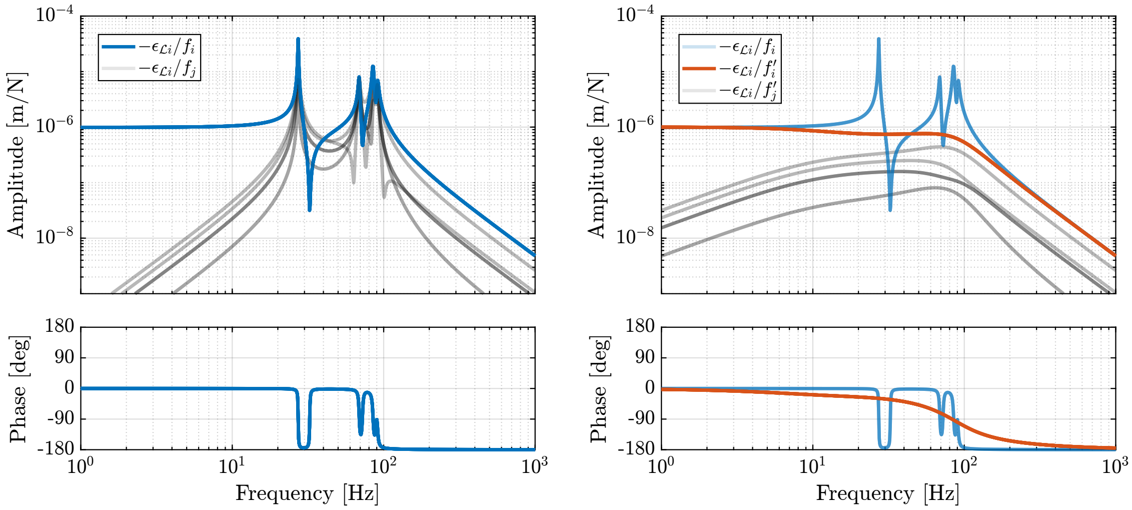

(a) Undamped plant in the frame of the struts

(b) Damped plant with Decentralized IFF

Figure 4.7: Plant in the frame of the strut for the High Authority Controller.

shown in Figure 4.8a.

$$\boldsymbol{K}_{\text{HAC}}(s) = \begin{bmatrix} K_{\text{HAC}}(s) & & 0 \\ & \ddots & \\ 0 & & K_{\text{HAC}}(s) \end{bmatrix}, \quad K_{\text{HAC}}(s) = g_0 \cdot \underbrace{\frac{\omega_c}{s}}_{\text{int}} \cdot \underbrace{\frac{1}{\sqrt{\alpha}} \frac{1 + \frac{s}{\omega_c/\sqrt{\alpha}}}{1 + \frac{s}{\omega_c\sqrt{\alpha}}}}_{\text{lead}} \cdot \underbrace{\frac{1}{1 + \frac{s}{\omega_0}}}_{\text{LPF}} \tag{4.2}$$

The stability of the MIMO feedback loop is analyzed through the *characteristic loci* method. Such characteristic loci, shown in Figure 4.8b, represent the eigenvalues of the loop gain matrix $\boldsymbol{G}(j\omega)\boldsymbol{K}(j\omega)$ plotted in the complex plane as frequency varies from 0 to ∞. For MIMO systems, this method generalizes the classical Nyquist stability criterion: with the open-loop system being stable, the closed-loop system is stable if none of the characteristic loci encircle the -1 point [4]. As seen in Figure 4.8b, all loci remain to the right of the -1 point, confirming the stability of the closed-loop system. Additionally, the distance of the loci from the -1 point provides information about stability margins for the coupled system.

Conclusion

The control architecture developed for the uniaxial and the rotating models has been adapted for the Stewart platform.

Two fundamental choices were first addressed: the selection between centralized and decentralized approaches, and the choice of control space. While control in Cartesian space enables direction-specific performance tuning, the implementation in strut space was selected for the conceptual design phase due to two key advantages: good decoupling at low frequencies and identical diagonal terms in the plant transfer functions, allowing a single controller design to be replicated across all struts.

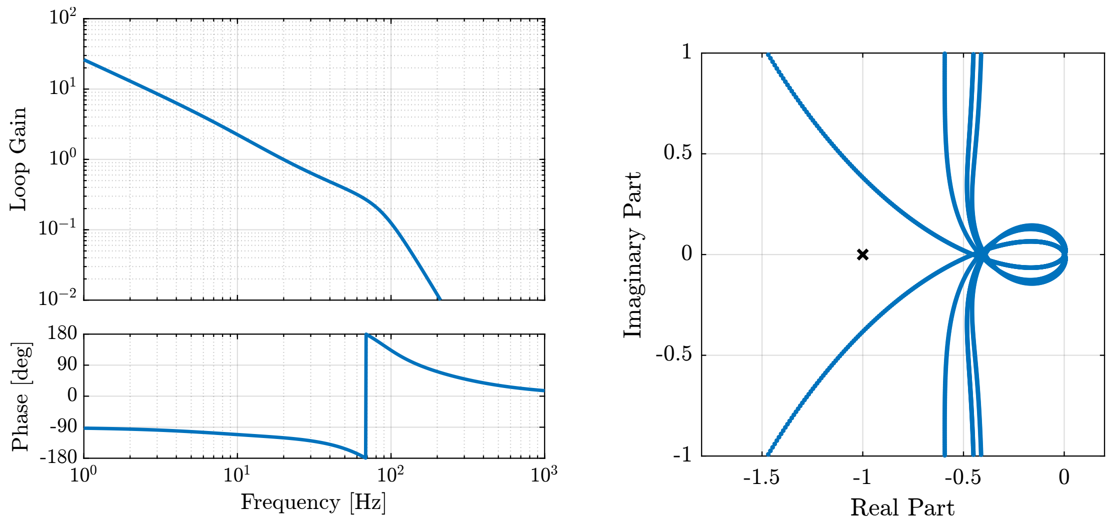

(a) Loop Gain

(b) Characteristic Loci

Figure 4.8: Decentralized HAC-IFF

The HAC-LAC strategy was then implemented. The inner loop implements decentralized Integral Force Feedback for active damping. The collocated nature of the force sensors ensures stability despite strong coupling between struts at resonance frequencies, enabling effective damping of structural modes. The outer loop implements High Authority Control, enabling precise positioning of the platform.

This control architecture will then be used for the conceptual validation of the NASS. More sophisticated control strategies will be investigated during the detailed design phase

Conclusion

- Configurable Stewart platform model
- Will be included in the multi-body model of the micro-station =¿ nass multi body model
- Control: complex problem, try to use simplest architecture

Bibliography

[1] H. Taghirad, *Parallel robots : mechanics and control*. Boca Raton, FL: CRC Press, 2013 (cit. on p. 4).

[2] D. Stewart, "A platform with six degrees of freedom," *Proceedings of the institution of mechanical engineers*, vol. 180, no. 1, pp. 371–386, 1965 (cit. on p. 6).

[3] A. Preumont, M. Horodinca, I. Romanescu, *et al.*, "A six-axis single-stage active vibration isolator based on stewart platform," *Journal of Sound and Vibration*, vol. 300, no. 3-5, pp. 644–661, 2007 (cit. on p. 19).

[4] S. Skogestad and I. Postlethwaite, *Multivariable Feedback Control: Analysis and Design - Second Edition*. John Wiley, 2007 (cit. on p. 25).

[5] A. Preumont, B. De Marneffe, and S. Krenk, "Transmission zeros in structural control with collocated multi-input/multi-output pairs," *Journal of guidance, control, and dynamics*, vol. 31, no. 2, pp. 428–432, 2008 (cit. on p. 23).